Journal of Materials Chemistry A



PAPER



Cite this: J. Mater. Chem. A, 2019, 7, 22092

Prussian blue-assisted one-pot synthesis of nitrogen-doped mesoporous graphitic carbon spheres for supercapacitors†

Arosha C. Dassanayake, Nilantha P. Wickramaratne, Mohammad Akter Hossain, Vindya S. Perera, Jacob Jeskey, Songping D. Huang, Hao Shen and Mietek Jaroniec *

Synthesis of nitrogen doped mesoporous graphitic carbon spheres with dispersed metal oxide nanoparticles using a single temperature treatment step serves as one of the big challenges in materials research. To date only a few reports have been published on the soft-templating synthesis of mesoporous graphitic carbons. The preparation of graphitic carbons with dispersed Fe_2O_3 using a single carbonization step at relatively low temperatures is yet to be explored. The first phase of this work shows the potential of graphitization of polyvinylpyrrolidine (PVP) stabilized cubic Prussian blue nanoparticles (CPB) in phenolic resin spheres to produce graphitic carbon spheres through a facile Stöber-like method. In the second phase, the Pluronic F127 soft template was used along with PVP stabilized Prussian blue nanoparticles (PB) in carbon spheres to generate mesopores and graphitic domains with uniformly dispersed Fe_2O_3 nanoparticles in these spheres. Due to the presence of graphitic layers, doped N species and Fe_2O_3 nanoparticles in the carbon matrix, the yielded carbon spheres feature a high surface area and magnetic properties. Moreover, these graphitic spheres exhibited excellent capacitive behavior with rectangular cyclic voltammetry (CV) profiles and large capacitance up to 247 F g^{-1} at 1 mV s^{-1} scan rate in 6 M KOH solution.

Received 3rd August 2019 Accepted 10th September 2019

DOI: 10.1039/c9ta08454a

rsc.li/materials-a

Introduction

Nanostructured carbons such as graphene, 3D-mesoporous carbons, carbon spheres, graphitic carbons, and carbon nanotubes have been vastly studied because of their potential industrial and medical applications.1 These nanostructured carbons are designed with special emphasis on the achievement of desired morphology, porous structure, functionalization, and graphitization. Specifically, porous graphitic carbons have been vastly studied for energy storage applications mainly due to their unique chemical and physical properties, such as, high conductivity, high surface area, good corrosion resistance, controlled pore structure, and most importantly, low cost.2 Graphene (hexagonally arranged one-atom thick planar carbon sheets³) has been one of the most studied materials for the last several years and shows superior electrochemical properties due to its unique structure. Graphene layers ensure high electron mobility, and their conductivity can be tuned via field effects.4 It was reported that graphitic carbons having a few

Department of Chemistry and Biochemistry, Kent State University, Kent, Ohio 44242, USA. E-mail: jaroniec@kent.edu; Fax: +1-330-672-3816; Tel: +1-330-672-3790

layers of graphene display graphene-like properties and their use as electrodes for supercapacitors has been widely studied.⁵⁻⁷ Recently, nitrogen doped mesoporous carbon spheres are intensively studied mainly due to their large surface area, tunable porosity accessible for electrolytes, superior conductivity and most importantly, their potential applications in the energy storage field.^{8,9} However, there are only a few reports devoted to the one-pot synthesis of mesoporous graphitic carbon spheres.

There are mainly three methods available for the synthesis of graphitic carbons: (1) high-temperature chemical vapor deposition (CVD), 3,10-13 (2) carbonization at high-temperature or/and high pressure14-16 and (3) catalytic graphitization.17-19 Among them, catalytic graphitization has been widely adopted due to its industrial feasibility. This method involves introduction of certain metallic species that possess the potential to convert surrounding amorphous carbon domains to graphitic carbons at elevated temperatures. So far, various metal species specifically of transition metals such as Cr, Mn, Fe, Co, Ni, Ti, V, Mo and W have been utilized as the graphitization catalysts. In the case of transition metal species, their catalytic properties have been attributed to their ability to accept electrons from positively charged dissolving carbon atoms during graphitization.20 Specifically, the electronic configuration of group VIII metals with their d orbitals occupied by 6-10 electrons is scarcely

 $[\]dagger$ Electronic supplementary information (ESI) available: Experimental sections describing materials, characterization, CO₂ measurements and calculations. See DOI: 10.1039/c9ta08454a

changed by accepting additional electrons from dissolving carbon atoms and therefore they act as efficient catalytic agents for graphitization. Fe, a member of group VIII with vacant d orbitals, serves as a promising candidate for catalytic graphitization.

Among various graphene morphologies mesoporous graphitic carbon spheres, also named as "graphene nanoballs", show an enhanced electron conductivity because of the presence of graphene nano-networks and available mesopores for ion transport.21 Lee and co-workers used CVD for the synthesis of graphene-like carbon particles as electrode materials for supercapacitors, 11 where the sulfonated poly(styrene-co-methacrylic acid) (SPS-COOH)/FeCl3 mixture was heated to 1000 °C under a H₂/Ar atmosphere followed by rapid cooling to room temperature for annealing and finally the iron species in the samples were removed by HCl etching to obtain graphene nanoballs. Yen and co-workers reported the Ni-vapor assisted growth of graphene nanoballs.13 In this work, graphitization was done at 950-1100 °C. Even though CVD appears to be a favorable way to obtain graphitic domains, it is obvious that this synthesis method is costly because of high temperature used. In addition, high graphitization temperatures above 1000 °C may result in the decomposition of functional groups such as heteroatoms (N and S) within the carbon structures, which in turn lowers the commercial value and the range of applications of these carbons. Furthermore, the CVD process prevents pore size tuning, addition of multiple components during the synthesis and operates at very high temperatures (>1000 $^{\circ}$ C) and low pressures. Therefore, CVD is less preferred from the industrial point of view.

Recently, spherical carbon and spherical metal-carbon composites have been synthesized using simple one-pot methods such as hydrothermal, soft templating and Stöberlike synthesis. These carbon spheres have received great attention from the scientific community because the spherical morphology improves their performance in various applications such as energy storage, 22,23 biomedicine, 4 adsorption, 25-28 optics and catalysis.29-32 Nanoparticles with spherical morphology are extensively used for energy storage due to their high surface area, short mass diffusion time and transport resistance. In drug delivery, it has been found that spherical nanoparticles are highly favored by cells over other morphologies during internalization.33 Despite extensive studies on carbon particles, to the best of our knowledge only a few attempts have been made to synthesize mesoporous graphene nanoballs using one-pot methods followed by a single step carbonization strategy.

Mesoporosity in graphitic carbons plays a vital role in charge propagation in the charging–discharging process. For instance, mesoporous carbons are widely used as materials for oxygen reduction. Hard templating, also known as nanocasting, is widely employed to introduce mesoporosity into carbon spheres. In this method, various types of hard templates such as silica particles, SBA-15 silica, CaCO₃ particles and polymer particles have been used. In many occasions removal of the template is associated with structural collapse and environmental hazards such as the usage of hazardous aqueous

ammonium bifluoride (NH₄HF₂), hydrogen fluoride (HF) or sodium hydroxide (NaOH) for the removal of silica templates.³⁹ Even though porosity can be tuned using such hard templates, there is a possibility of damaging the carbon framework by the chemicals used. On the other hand, the hard-templating strategy forbids incorporation of metal nanoparticles into carbons since such metals are removed during the template removal process as well. In relation to the production of mesoporous graphitic carbons with incorporated metal nanoparticles, the hard-templating strategy is not feasible.

Bang demonstrated the synthesis of hollow graphitic carbon spheres in the presence of decyltrimethylammonium bromide as a soft template, pyrrole as a carbon precursor and FeCl₃ as a graphitization catalyst.40 A similar type of soft-templating approach has been employed by Wang and co-workers to synthesize hierarchical porous graphitic carbon spheres using F127 as a template, and Co(II) gluconate as a carbon/metal precursor.41 Several studies reported the synthesis of capacitive monolayer type carbons using self-assembled micelles of F127. 42,43 Recently, we have shown a simple one-pot synthesis of 3-D mesoporous graphitic carbons in the presence of PB as a graphitization catalyst.44 We also showed that graphitization of the PVP-coated PB in the mesoporous resorcinolformaldehyde-derived carbon can be achieved at 700 °C along with a high yield (87%) of graphitic domains. Another report⁴⁵ shows the synthesis of graphitic carbon particles using PB as a graphitization catalyst. However, in this case the postsynthesis strategy was used to incorporate the PB particles, which makes this synthesis more complicated. However, there is no report showing a simple one-pot synthesis of mesoporous graphitic carbon particles using PB as a graphitization catalyst.

In the current study, we elaborate an effective one-pot Stöberlike synthesis of graphitic carbon spheres in the presence of two types of PVP-stabilized PB nanoparticles as graphitization catalysts. In the first series of carbons, single cubic PB nanoparticles are used as cores, which are coated with phenolic resin shells. These core-shell particles upon carbonization under a nitrogen atmosphere at 600 °C are converted to graphitic carbon particles with incorporated iron oxide nanoparticles. The second series of carbons was produced by incorporating comparatively smaller PB nanoparticles along with the mesopore generating Pluronic F127 soft template into resol polymer spheres, which upon carbonization generated mesoporous graphitic carbon spheres with dispersed iron oxide nanoparticles. Testing the supercapacitance of these mesoporous graphitic spheres showed their excellent capacitive behavior and cycle stability. From the industrial viewpoint, these graphitic carbon particles could serve as novel, economical and reliable materials for a range of applications such as energy storage, adsorption, and biomedicine.

Experimental

Characterization of carbon spheres and calculations

Detailed information about all chemicals, techniques and instrumentation used for the preparation and characterization of all carbon samples is provided in the ESI.† Characterization

of the materials was performed by using nitrogen adsorption, scanning electron microscopy (SEM-Quanta-450), transmission electron microscopy (TEM-Tecnai G2 F20), elemental analysis (LECO TruSpec Micro Elemental Analyzer), Raman spectroscopy (Horiba LabRam HR-800) and thermogravimetry (TGA Q-500 analyzer: TA Instruments, Inc., New Castle, DE). Information on the evaluation of the BET specific surface area, the volumes of micropores and mesopores, pore widths, and pore size distributions (PSDs) is provided in the ESI.†

Electrochemical measurements

A three-electrode system was utilized to evaluate the electrochemical performance of the synthesized carbon spheres. To prepare the working electrode, \sim 1 mg of the carbon spheres was dispersed in 1 mL of 1:3 water/ethanol mixture followed by addition of 4 µL of 0.5 wt% Nafion perfluorinated resin solution (Sigma-Aldrich). The mixture was sonicated for an extended period for achieving an optimal dispersion. 5 µL of the suspended mixture was added to a glassy carbon electrode (3 mm in diameter, CH Instrument) and air dried. This working electrode, along with a Pt wire counter electrode, and an Ag/AgCl reference electrode formed a three-electrode system. Cyclic voltammograms were collected under various scan rates (1 to 100 mV s⁻¹) using a potentiostat (CHI1200C, CH instruments). 6 M KOH was used as the electrolyte for the capacitance measurements, while 110 µM resazurin in 50 mM phosphate buffer (pH = 7.3) was used for the measurement of redox activities.

Synthesis of PVP coated cubic Prussian blue nanoparticles

Cubic Prussian blue (CPB) nanoparticles were obtained following the method reported by Yamauchi *et al.*,⁴⁶ Briefly, 3.00 g of PVP and 132 mg of $K_3[Fe(CN)_6] \cdot 3H_2O$ were added to 40 mL of 0.01 M HCl solution under magnetic stirring. The reaction mixture was stirred for 30 min at room temperature. The resulting reaction mixture was then heated in an oven at 80 °C for 20 h. The product was separated by centrifugation and washed several times with the water and ethanol mixture (1 : 3).

Synthesis of composite CPB-carbon spheres

Composite CPB-carbon spheres were obtained through a onepot hydrothermal method. In a typical synthesis, an aqueous solution of CPB was prepared by mixing 0.1 g of CPB and 20 mL of deionized water. The resulting suspension was sonicated for ca. 1 min and stirred magnetically for 20 min until CPB nanoparticles were completely immersed. Next, ethanol (8 mL) was added and the mixture was stirred for another 5 min. Thereafter, resorcinol (0.2 g) was added and stirred for 30 min. Subsequently, 25 wt% ammonia (0.2 mL) was added under continuous stirring for 30 min. It was followed by an addition of 0.3 mL of 37 wt% formaldehyde and the resultant mixture was transferred into a 125 mL capacity autoclave vessel, which was then placed in a metal autoclave vessel inside a 100 °C oven for 24 h. The resulting solid product (CPB-polymer spheres) was obtained by centrifugation and dried at 100 °C for 12 h. The resulting polymer spheres were labeled as PSCPB.

To prepare carbon spheres, the aforementioned polymer spheres were subjected to the thermal treatment under a $\rm N_2$ environment. Specifically, the PSCPB material was placed in a tube furnace and heated at a rate of 2 °C min⁻¹ up to 350 °C. After dwelling for 4 h, heating was resumed at a rate of 5 °C min⁻¹ up to a final temperature of 500–600 °C, followed by another dwelling for 2 h. The resulting carbon spheres were labeled as CSCPB-T; symbol "T" refers to the initial digit of carbonization temperature, whereas "PS", "CS" and "CPB" refer to polymer spheres, carbon spheres and cubic Prussian blue, respectively. For instance, CSCPB-6 refers to the carbon spheres with CBP nanoparticles graphitized at 600 °C.

Synthesis of Prussian blue nanoparticles

A 30 mM aqueous solution of FeCl $_3$ (100 mL) was added to the mixture of a 30 mM aqueous solution of $K_4[Fe(CN)_6]$ (100 mL) and PVP (average MW = 40 000, 0.8325 g) under vigorous stirring. The reaction mixture was then stirred for about 1 h. The reaction product was dialyzed using the regenerated cellulose tubular membrane (MWCO is 12 000–14 000) against distilled water for 2 days. The solid product was collected by lyophilization of the above solution.

Synthesis of ordered mesoporous carbon spheres

First, phenol (0.8 g) was dissolved in 0.1 M NaOH solution (20 mL). Then 37 wt% formaldehyde (2.8 mL) was added and heated at 70 °C under stirring for 30 min. A separate solution was prepared by dissolving Pluronic F127 (1.28 g) in 15 mL of deionized water. Later, this solution was added to the phenolic solution dropwise under gentle stirring. The resulting mixture was stirred for 2 h, diluted with 50 mL of deionized water and stirred for an additional 18 h. The resulting pink solution was further diluted with 255 mL of deionized water and autoclaved at 130 °C for 10 h. The resulting polymer spheres were dried at 60 °C overnight and carbonized under N2. In detail, polymer spheres were placed in a tube furnace and heated at a rate of 1 °C min⁻¹ up to 350 °C, followed by dwelling for 2 h. Next, heating was resumed at a rate of 1 °C min⁻¹ up to a desired final temperature (600/700/800 °C), followed by dwelling for another 2 h. The resulting ordered mesoporous carbon spheres (OMCS) were labeled as OMCS-x, where "x" denotes the final carbonization temperature, respectively.

Synthesis of ordered mesoporous graphitic carbon spheres

Synthesis of ordered mesoporous graphitic carbon spheres (OMGCS) was carried out by adopting a similar strategy to the synthesis of OMCS, modified by adding PB nanoparticles (0.1 g) to the F127 solution before mixing with phenolic solution. The resulting product after carbonization was labeled as OMGCS-x, where "OMGCS" and "x" denote ordered mesoporous graphitic carbon spheres and final carbonization temperature, respectively.

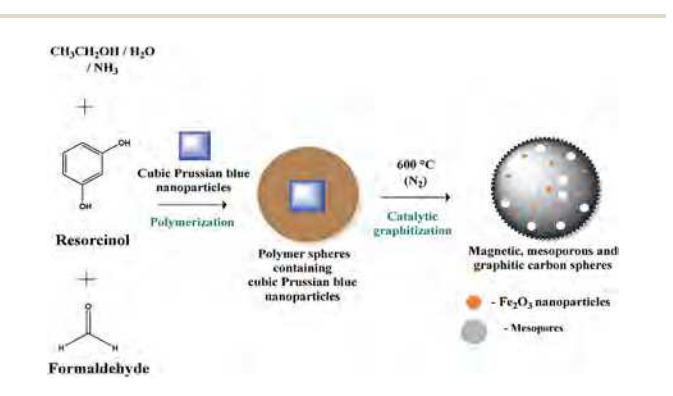
Results and discussion

Morphology

Carbon particles with CPB cores and phenolic resin shells were synthesized using a sol-gel method in the presence of PVP coated CPB nanoparticles, resorcinol, formaldehyde, and NH₃ in the ethanol-water mixture as shown in Scheme 1. Graphitic carbon spheres were obtained by carbonization of polymer spheres under a N2 atmosphere. The SEM and TEM images of the as-synthesized polymer and graphitic carbon spheres are shown in Fig. 1a(i-vi). As can be seen, all polymer and graphitic carbon particles possess a spherical morphology with the mean diameters around 100 nm. As shown in Fig. 1a(i and ii), the CPB structure has been preserved during the synthesis of polymer spheres. Usually PB particles are unstable under a basic environment,47 which could lead to the deterioration of CPB particles and their morphology. However, the current study shows that the controlled coating of the CPB surface with phenolic resins can protect the CPB morphology under basic conditions. The formation of this core-shell structure can be attributed to the favorable interactions between hydrophilic PVP on the CPB core and hydrophilic resorcinol-formaldehyde shell. First, hydrophilic PVP-CPB particles were well dispersed in the waterethanol solution and then resorcinol was introduced into the system. The added resorcinol is accumulated on the PVP stabilized CPB cores due to their hydrophilic nature. The resorcinol coating on the CPB cores protects them against alkaline medium and prevents the penetration of alkaline species through the resorcinol layer.

Addition of formaldehyde and ammonia resulted in the formation of resorcinol-formaldehyde resin, which forms shells around the CPB cores. This further hinders the contact between alkaline species and CPB cores. It is noteworthy that in general this PVP coating strategy would enable the incorporation of metal species during Stöber synthesis, which otherwise would be precipitated as respective hydroxides in ammonia medium.

The cubic morphology of the CPB core was destroyed during the carbonization process. It has been previously shown that CPB particles are not stable at elevated temperatures and it has been further stated that they can be converted to metallic iron and iron oxides at high temperatures.44,48 As shown in



Scheme 1 Schematic illustration of the synthesis of graphitic mesoporous carbon spheres.

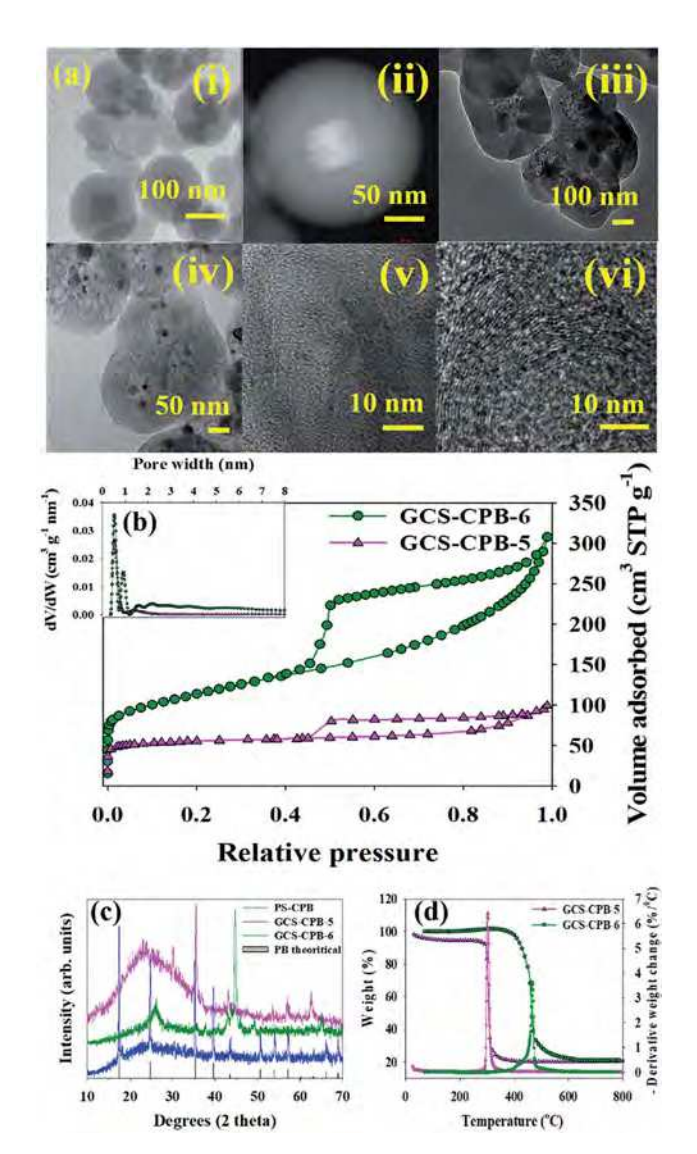


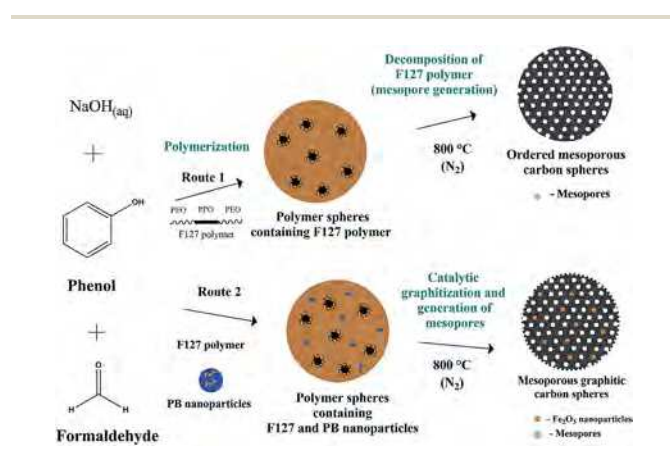
Fig. 1 High-resolution transmission electron microscopy (HRTEM) images: (a-i) PS-CPB, (a-ii) contrast image of PS-CPB, (a-iii) GCS-CPB-5, (a-iv) GCS-CPB-6, and (a-v and vi) magnified images of GCS-CPB-6. (b) N₂ adsorption isotherms and respective pore size distributions (PSDs; V denotes the volume adsorbed and W the pore width). (c) X-ray diffraction (XRD) patterns and (d) thermogravimetric (TG) and differential TG profiles (DTG) of the samples recorded in air.

Fig. 1a(iv), the CPB cores were fragmented into nanosized metallic iron and/or iron oxide particles, which are well scattered through the carbon particles. The sizes of these metallic particles range from 1 nm to 20 nm. The magnified HRTEM images of GCS-CPB-6 were obtained to study their graphitic nature. As shown in Fig. 1a(v and vi), the GCS-CPB-6 sample possesses graphitic domains with nicely stacked graphene layers (5 to 20 layers). As previously shown,44 these smaller graphitic domains in the carbon particles can exhibit graphenelike properties. The carbon obtained at 500 °C contained both cubic shaped metallic species, which resemble the initial CPB cores, and the fragmented iron species. This clearly indicates that the decomposition of CPB started at around 500 °C.

Even though graphitic spheres were produced from CPB incorporated polymer spheres, the resulting carbons show aggregated Fe_2O_3 particles around the graphitic domains and feature a broad distribution of mesopores. However, larger iron oxide nanoparticles possess a smaller surface area, which hinders their contribution to the overall capacitance in the composite materials. The main reason behind aggregation of Fe_2O_3 is the use of single CPB cores in the resulting core–shell particles. Furthermore, the synthesis route shown in Scheme 1 does not allow for the formation of the ordered mesoporosity. Therefore, the second series of carbon spheres was prepared as shown in Scheme 2, where Pluronic F127 was used to generate mesopores while smaller PB nanoparticles were used to generate graphitic domains throughout the carbon spheres ensuring better Fe_2O_3 dispersion.

First, ordered mesoporous carbon spheres (OMCS) were synthesized using an appropriate mass of Pluronic F127 block copolymer. Pluronic F127 is one of the well-studied soft templates used to generate mesopores within carbons due to its decomposition at higher carbonization temperatures. 49-55 It was shown that lower (1.11 g) and higher (1.37 g) masses of F127 failed to generate monodispersed carbon particles with smooth surfaces (see Fig. S1a and b in the ESI†). Interestingly, carbonization temperature has a pronounced effect on the morphology and porosity of the resulting particles. As can be seen from Fig. 2a, carbonization at 600 °C was insufficient to remove completely the F127 polymer, which resulted in large carbon spheres with noticeable aggregation of particles in the OMCS-6 sample. Furthermore, no intra-particle mesoporosity was observed based on the TEM images (see Fig. 2b). In contrast, carbonization at 700 °C (Fig. 2c) generated particles with smaller aggregation and mesopores formed inside the resulting OMCS-7 particles (Fig. 2d). However, the mesopores inside OMCS-7 were not well ordered. Therefore, another batch was obtained at 800 °C (OMCS-8). Interestingly, carbonization at 800 °C resulted in the formation of monodisperse spheres with ordered mesoporosity (see Fig. 2f).

Amidst several studies conducted so far on one-pot synthesis of ordered mesoporous carbon spheres (OMCS) using F127 as



Scheme 2 Synthesis route to obtain ordered mesoporous carbon spheres (OMCS) and mesoporous graphitic carbon spheres (OMGCS).

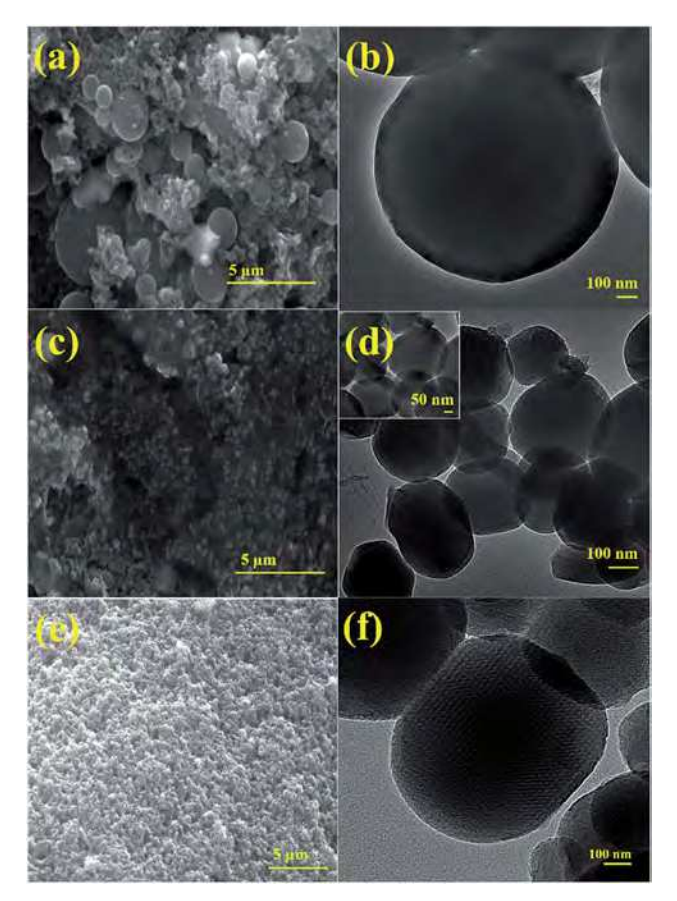


Fig. 2 Scanning electron microscopy (SEM) images of (a) OMCS-6, (c) OMCS-7, and (e) OMCS-8 and transmission electron microscopy (TEM) images of (b) OMCS-6, (d) OMCS-7, and (f) OMCS-8.

a soft template, only a few of them were extended toward their graphitization. In the current study, OMCS were graphitized by incorporating PVP coated PB nanoparticles to produce graphitic mesoporous carbon spheres (OMGCS). TEM images of OMGCS reveal the presence of graphitic domains with well-dispersed Fe_2O_3 nanoparticles within the resulting structures (see Fig. 4d and f). Sizes of these Fe_2O_3 nanoparticles were estimated to be around 20 nm. However, further carbonization at 900 °C (OMGCS-9) seems to cause a partial collapse of the carbon structure due to excessive graphitization (see Fig. S1c in the ESI†).

XRD and Raman studies

The crystallinity of the samples was evaluated using wide-angle XRD measurements. The distinct peaks at $2\theta=17.5^{\circ}$, 24.8° , 35.3° and 39.6° for PS-CPB polymer spheres can be assigned to the crystalline PB structure (see Fig. 1c), which is well evidenced by overlapping with PB theoretical peaks at the same 2θ values. The diffraction peaks for GCS-CPB-5 resemble the peaks obtained for PS-CPB, further indicating the presence of CPB in GCS-CPB-5. In addition, it exhibits other peaks around $2\theta=43.5^{\circ}$ and 53.9° , which can be attributed to the reflections from γ -Fe₂O₃. Diffraction peaks for GCS-CPB-6 at $2\theta=26^{\circ}$ can be indexed as reflections from the (002) planes of graphitic carbon

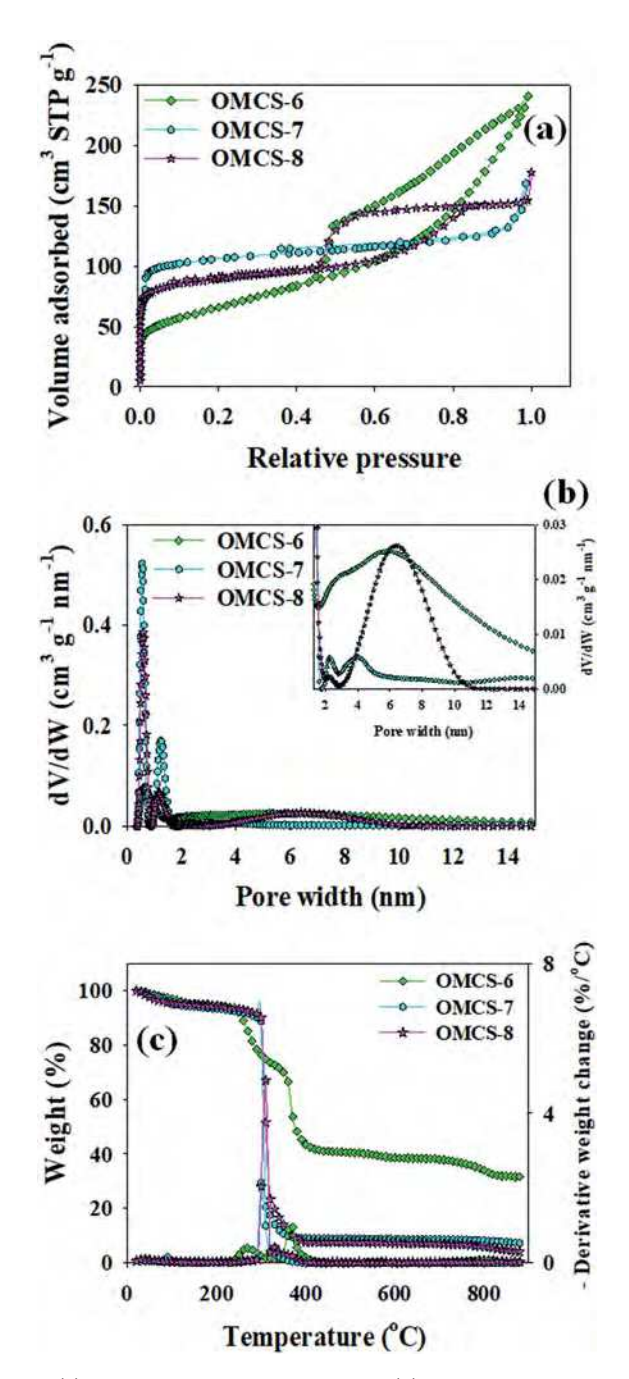


Fig. 3 (a) $\rm N_2$ adsorption isotherms and (b) pore size distributions (PSDs) of the OMCS-6, OMCS-7 and OMCS-8 samples. Symbol V denotes the volume adsorbed and W the pore width.

(see Fig. 1c). The broad diffraction patterns at $2\theta=26^\circ$ for GCS-CPB-5 are characteristic of amorphous carbons. Interestingly, GCS-CPB-6 has a comparatively strong broad peak at $2\theta=26^\circ$, indicating the presence of graphitic domains with a few layers of 2D-graphene structures. Similar strong peaks were observed for OMGCS-8 and OMGCS-9 samples (see Fig. 5e), corresponding to diffraction patterns from 002 and 101 graphitic planes observed at 26° and 43° respectively. In contrast to the GCS-CPB-6 sample, strong peaks for graphitic carbon are not observed for the OMGCS-6 sample.

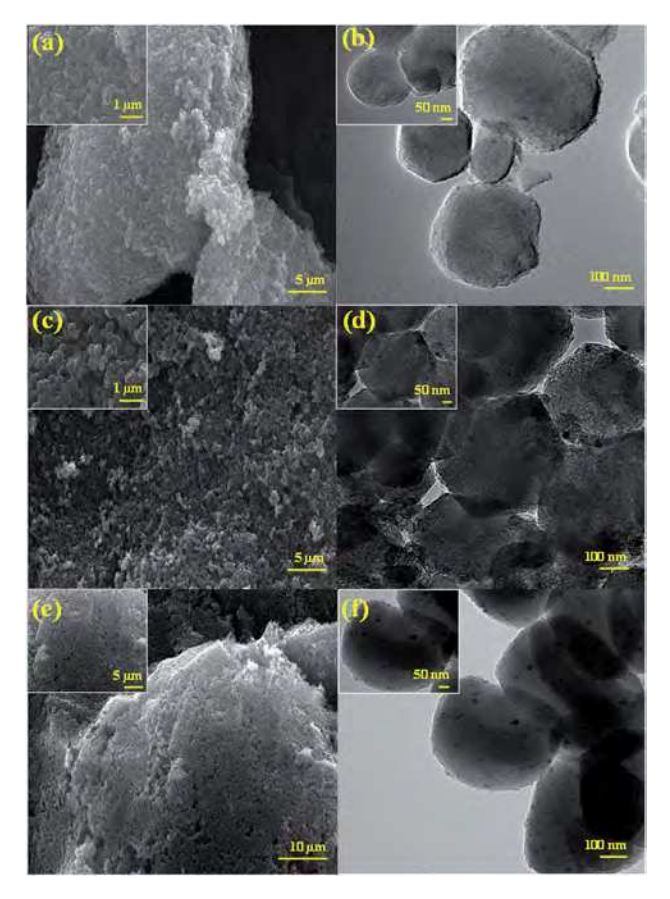


Fig. 4 Scanning electron microscopy (SEM) images of (a) OMGCS-6, (c) OMGCS-7, and (e) OMGCS-8 and transmission electron microscopy (TEM) images of (b) OMGCS-6, (d) OMGCS-7, and (f) OMGCS-8.

As shown in our previous report,44 the PB particles act as catalysts for low temperature graphitization. Furthermore, the diffraction peaks centered at $2\theta = 35.6^{\circ}$, 43.5° and 53.9° in the XRD patterns obtained for the carbon samples can be assigned to γ -Fe₂O₃. It is noteworthy that a broad peak observed at \sim 43– 44° in the XRD patterns collected for the GCS-CPB-6, OMGCS-7 and OMGCS-8 samples can be ascribed to an overlapping of the strong (101) reflection (JCPDS no. 75-1621) of the graphitic carbon with the (400) reflection of γ -Fe₂O₃ (JCPDS no. 89-5892). In addition, the sharp peak at $2\theta = 44.7^{\circ}$ for GCS-CPB-6 can be assigned to the (110) plane of the α -Fe phase. The particle sizes of γ -Fe₂O₃ and α -Fe₂O₃ in the GCS-CPB-6 sample estimated using Debye-Scherrer's equation are 17 nm $(2\theta = 35.6^{\circ})$ and 74 nm $(2\theta = 44.7^{\circ})$, respectively. These particle sizes are comparable with those obtained from the TEM images (see Fig. 1a(iv)). The thickness of the graphitic domains in GCS-CPB-6 was found to be 3.7 nm. Thus, the average number of graphene layers in nanoballs is estimated to be about 11, given that the distance between two graphene layers is 0.34 nm.

Raman spectroscopy measurements were performed for the OMCS-8 and OMGCS-9 samples to get more information about graphitization degree (see Fig. 5f). Both OMCS-8 and OMGCS-9 samples exhibited characteristic D and G bands around 1340 cm⁻¹ and 1580 cm⁻¹, respectively. The G band, likely

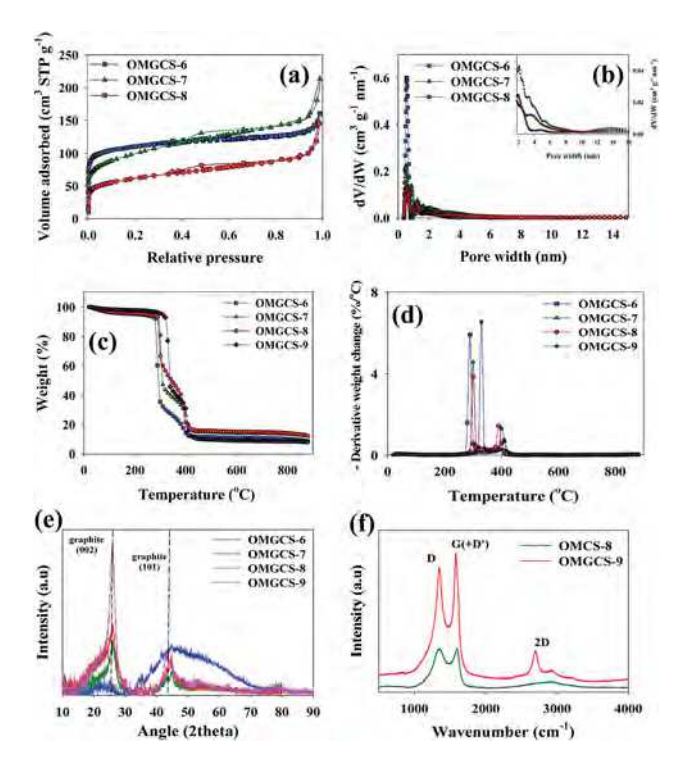


Fig. 5 (a) N_2 adsorption isotherms, (b) pore size distributions (PSDs; V is the volume adsorbed, and W is the pore width), (c) thermogravimetric (TG) profile recorded in air, (d) differential thermogravimetric (DTG) profile, (e) X-ray diffraction (XRD) patterns and (f) Raman spectra of the samples studied.

a combination of G and D' bands, arises from the $\rm E_{2g}$ vibrations of the C–C bond stretching of graphene sheets. The D band observed at 1350 cm⁻¹ arises from the $\rm A_{1g}$ vibrational mode corresponding to amorphous carbon. ^{56,57} The peak ratio of the G and D bands ($I_{\rm G}/I_{\rm D}$) for the OMCS-8 and OMGCS-9 samples is 1.00 and 1.11, respectively. The higher $I_{\rm G}/I_{\rm D}$ value for the OMGCS-9 sample further confirms the presence of graphitic domains as compared to those in OMCS-8.

Thermogravimetric analysis

Thermogravimetric analysis (TG) profiles obtained in air are shown in Fig. 1d and 3c. The oxidation temperatures for GCS-CPB-5 and GCS-CPB-6 are 304 °C and 467 °C, respectively. It is known that graphitic carbons have higher thermal stability than amorphous carbons in an oxygen-containing atmosphere. Therefore, the higher oxidation temperature observed for GCS-CPB-6 is mainly due to its graphitic nature, which has also been confirmed by TEM and XRD analysis. GCS-CPB-5 is mainly composed of amorphous carbons. This also confirms that the catalytic graphitization is initiated at temperatures above 500 °C. The TG profiles for both GCS-CPB-5 and GCS-CPB-6 samples recorded in air show a constant residue of 20% at 750 °C and above, which can be assigned to the remaining iron species after oxidation of the entire carbon.

PS-CPB holds 8.1% of elemental nitrogen, the source of which is mainly nitrogen-rich PVP and CN containing PB.

Interestingly, both the GCS-CPB-5 and GCS-CPB-6 samples were able to retain a comparable fraction of nitrogen during the high temperature carbonization process. Namely, GCS-CPB-5 and GCS-CPB-6 retained up to 1.67% and 0.60% of nitrogen, respectively. It is obvious that CPB-6 contains less nitrogen as compared to CSPB-5 because its carbonization temperature was higher (600 $^{\circ}$ C νs . 500 $^{\circ}$ C).

Graphitic mesoporous carbons (OMGCS) exhibited two distinct decomposition peaks in their differential thermogravimetric (DTG) profiles, one peak at temperatures below 330 °C and the other above 380 °C. Therefore, the degree of graphitization of each sample was calculated using eqn (1).

Graphitic carbon % =

$$\frac{\text{graphitic carbon weight loss \%}}{(\text{graphitic} + \text{amorphous}) \text{carbon weight loss}} \times 100 \quad (1)$$

The remaining weight percentages at 900 $^{\circ}$ C correspond to metal oxides formed dring heating in air. As expected, the degree of graphitization of the samples increases from 13.2% to 32.2% with increasing carbonization temperature from 600 $^{\circ}$ C to 800 $^{\circ}$ C. The values of the graphitization degree and metal oxide percentage for the OMGCS-x samples are shown in Table 2.

Gas adsorption studies

Nitrogen adsorption isotherms and pore size distribution curves of GCS-CPB-x, OMCS-x and OMGCS-x samples are presented in Fig. 1b, 3a, b and 5a, b, respectively. All the parameters, the BET specific surface area, and pore structure parameters are listed in Table 1 (GCS-CPB-x) and Table 3 (OMCS-x and OMGCS-x). As shown in Fig. 1b, 3b and 5a, GCS-CPB-5, GCSCPB-6, OMCS-6, OMCS-8, OMGCS-6 and OMGCS-7 samples exhibit type IV isotherms with distinct hysteresis loops of H2(b) type showing delayed desorption.⁵⁸ These isotherms are characteristic of mesoporous materials. However, the closure of hysteresis loops at relative pressures around ~0.45 is mainly due to the presence of constricted mesopores.58 Inspection of adsorption isotherms measured for OMCS-6, OMCS-7 and OMCS-8 shows the effect of carbonization temperature on the mesopore formation. The H4 type hysteresis loop obtained for OMCS-6 indicates that mesopores were formed because of particle aggregation. The hysteresis loop collected for the OMCS-7 sample is a transitional loop between

 $\begin{tabular}{lll} \begin{tabular}{lll} \begin{$

Sample	$V_{\rm t}$ (cm ³ g ⁻¹)	$V_{\rm mi}$ (cm ³ g ⁻¹)	$V_{\rm me}$ (cm ³ g ⁻¹)	S_{BET} (m ² g ⁻¹)	N (wt%)
PS-CPB	_	_	_	_	8.61
GCS-CPB-5	0.15	0.07	0.08	194	1.67
GCS-CPB-6	0.45	0.10	0.35	397	0.60

 $[^]a$ $V_{\rm t}$ – total pore volume, $V_{\rm mi}$ – micropore volume (pores < 2 nm), $V_{\rm me}$ – mesopore volume (pores between 2 and 50 nm), $S_{\rm BET}$ – BET surface area.

Table 2 Decomposition temperatures, degree of graphitization and Fe_2O_3 percentage for the samples studied

Sample	T_1 (°C)	T_2 (°C)	Degree of graphitization (%)	Fe ₂ O ₃ (wt%)
OMCS-6	266			
OMCS-7	300			
OMCS-8	309			
OMGCS-6	292	392	13.2	8.7
OMGCS-7	298	388	16.3	12.0
OMGCS-8	300	488	29.6	12.4
OMGCS-9	329	402	32.2	8.0

H4 to H2(a) types. In the case of OMCS-8 its hysteresis loop shows H2(a) type, which indicates the presence of intra-particle mesopores with narrow pore openings. Furthermore, the pore size distribution obtained for OMCS-8 reveals the presence of uniform ordered mesopores with narrow distribution.

As can be seen from Fig. 1b and Table 1, GCS-CPB-6 possesses a comparatively high surface area and total pore volume of 397 $\mathrm{m^2~g^{-1}}$ and 0.45 $\mathrm{cm^3~g^{-1}}$, respectively, while GCS-CPB-5 has a relatively low surface area and pore volume of 194 m² g⁻¹ and $0.15 \text{ cm}^3 \text{ g}^{-1}$, respectively. It is obvious that higher carbonization temperature in the case of GCS-CPB-6 (600 °C vs. 500 °C) enhanced its microporosity and surface area. However, its large pore volume is mainly due to the presence of larger mesopores created during the graphitization process. The wider pore size distribution obtained for GCS-CPB-6 (see the inset in Fig. 1b) is due to the formation of internal voids caused by the transformation of amorphous carbon to graphitic one during catalytic graphitization. The sizes of mesopores created during graphitization range from 2 nm to 20 nm. These large mesopores are responsible for the larger pore volume of GCS-CPB-6. The small hysteresis loop observed for GCS-CPB-5 can be ascribed to its mesoporosity because of the presence of both inter-particle voids and constricted mesopores. The absence of large mesopores in GCS-CPB-5 is also an indication of its amorphous nature.

Graphitization of ordered mesoporous carbon spheres (OMCS) caused a gradual deterioration of ordered mesoporosity in the OMGCS-6, OMGCS-7 and OMGCS-8 samples (see Fig. 5b).

Table 3 Adsorption parameters and nitrogen percentage of the samples studied a

Sample	$S_{ m BET} \ ({ m m}^2{ m g}^{-1})$	$V_{\rm mi}$ (cm ³ g ⁻¹)	$V_{\rm me}$ (cm ³ g ⁻¹)	$V_{\rm tot}$ (cm ³ g ⁻¹)	<i>N</i> (wt%)
OMCS-6	235	0.05	0.30	0.35	
OMCS-7	368	0.16	0.09	0.25	
OMCS-8	300	0.12	0.13	0.25	
OMGCS-6	387	0.16	0.08	0.24	3.7
OMGCS-7	354	0.12	0.20	0.32	3.2
OMGCS-8	219	0.08	0.14	0.22	2.5

 $[^]a$ $V_{\rm t}$ – total pore volume, $V_{\rm mi}$ – micropore volume (pores < 2 nm), $V_{\rm me}$ – mesopore volume (pores between 2 and 50 nm), and $S_{\rm BET}$ – BET specific surface area.

Furthermore, the surface areas of these samples decrease from 387 m² g⁻¹ (OMGCS-6) to 219 m² g⁻¹ (OMGCS-8) with increasing graphitization temperature. Obviously, diminution of micropores increases with increasing graphitization of the samples. It is noteworthy that potassium species in the PB particles initiate *in situ* graphitization during carbonization, which is independent of catalytic graphitization. Note that higher and lower masses of PB than 0.100 g used in the synthesis of spheres affected the spherical morphology of OMGCS-PB0.075-8 and caused a partial structural collapse of OMGCS-PB0.200-8 (see Fig. S2 in the ESI†).

Interestingly, both GCS-CPB-5 and GCS-CPB-6 samples showed magnetic properties. As can be seen in Fig. S3 (ESI†), the water suspended samples could be easily separated from the solution upon exposure to an external magnetic field. Considering their magnetic properties, surface area, and particle size, these carbon particles can be used not only as adsorbents for the removal of pollutants from contaminated water but also as a drug carrier in biomedicine. Recently, magnetic particles have been vastly studied as drug carriers because these particles can be guided using an external magnet to desired locations of the body or tissue. 59,60

Electrochemical studies

Graphene-like carbon nanoballs are vastly studied for supercapacitor applications. For instance, graphitic carbons feature better electrical conductivity; the mesoporous structure facilitates

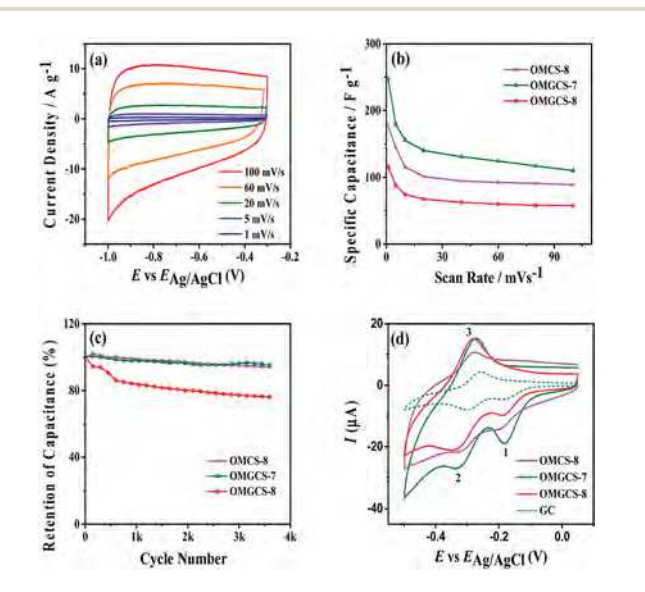


Fig. 6 Electrochemical performance of OMCS and OMGCS. (a) Cyclic voltammograms of OMGCS-7 in 6 M KOH using various scan rates. (b) The scan rate dependent specific capacitances. The slowest scan used was 1 mV s $^{-1}$, and the corresponding specific capacitances are 176 F g^{-1} , 247 F g^{-1} , and 116 F g^{-1} for OMCS-8, OMGCS-7, and OMGCS-8, respectively. (c) Cycling stabilities of OMCS-8, OMGCS-7, and OMGCS-8 measured at 100 mV s $^{-1}$ in 6 M KOH solution. Each sample was scanned for 3700 cycles. (d) Electrocatalyzed redox of resazurin. Each cyclic voltammogram has three redox peaks, which correspond to the irreversible reduction of resazurin (1) and the reversible redox between resorufin and dihydroresorufin (2 and 3).

the transportation of ionic electrolyte to the carbon surface, nitrogen and metal contents enhance the capacitance through pseudocapacitive reactions, and the microporous structure can hold more ions on the surface. The capacitive performance of OMCS, OMGCS-7 and OMGCS-8 was studied (see ESI†). The synthesized OMCS and OMGCS materials exhibit very good electrochemical performance. For instance, we measured the specific capacitance of carbon particles by performing cyclic voltammetry in 6 M KOH solution. All carbon spheres exhibited quasi-rectangular cyclic voltammograms up to 100 mV s $^{-1}$ (Fig. 6a and S4 in the ESI†), suggesting that they acted as electrochemical double-layer capacitors. 61,62 The specific capacitance was calculated using the following equation,

$$C = \frac{\int i \mathrm{d}V}{2V_{\mathrm{s}} \Delta V} \tag{2}$$

where $\int i dV$ is the integrated area under the cyclic voltammogram, V_s the scan rate, and ΔV the scan range. The as-prepared OMCS-8 exhibited 176 F g^{-1} and 145 F g^{-1} specific capacitance at a scan rate of 1 mV s⁻¹ and 5 mV s⁻¹, respectively (Fig. 6b). These values are comparable to those of other carbon-based capacitor materials reported previously, for instance, 3D graphene-based frame-works, 63 graphitic carbon spheres, 45 and mesoporous carbons.⁶⁴ Such high capacitance stems from the highly exposed area of OMCS-8 to the electrolyte solution. The hierarchical porous structure of OMCS-8 facilitates the diffusion and accumulation of ions as well. Carbonization of PB incorporated carbons at 700 °C (OMGCS-7) further improved the specific capacitance, and the overall conductivity of the sample increased upon graphitization. Therefore, OMGCS-7 exhibits 247 F g^{-1} and 179 F g^{-1} specific capacitance at a scan rate of 1 mV s^{-1} and 5 mV s^{-1} , respectively (Fig. 6b). Furthermore, the OMGCS-7 sample exhibited excellent capacitance retention. Its capacitance remained at 110 F g^{-1} at 100 mV s^{-1} , suggesting that the mesopores have improved the ion transport limit. These results are comparable with those obtained for yolk-shelled carbon spheres⁶⁵ or other nanohybrid supercapacitors. 66,67 The specific capacitances for all the mesoporous carbon materials studied in this work are summarized in Table S1 in the ESI.† For both OMCS-8 and OMGCS-7, they retained 96% of their original capacitances after 3700 scanning cycles (Fig. 6c). In contrast, carbonization at 800 °C (OMGCS-8) decreased the specific capacitance to 116 F g⁻¹ at 1 mV s⁻¹ (Fig. 6b), probably due to the partial collapse of the porous structure as confirmed by the BET surface area and pore volume results (Table 3). Moreover, the OMGCS-8 sample only retains 76% of its original capacitance after 3700 cycles (Fig. 6c), suggesting that this sample was less stable as a supercapacitor material as compared to OMCS-8 and OMGCS-7.

The OMCS and OMGCS samples also performed well as electrocatalysts. Fig. 6d shows the electrochemical redox of a well-known probe, resazurin. This probe is irreversibly reduced to a fluorescent product resorufin (peak 1 in Fig. 6d), which is further reduced to dihydroresorufin (peak 2 in Fig. 6d). The second stage reduction is reversible, and thus dihydroresorufin could be oxidized back to resorufin (peak 3 in Fig. 6d). This

probing reaction was utilized to evaluate the electrochemical activities of carbon-based materials in the past. 68,69 It is found that OMCS and OMGCS exhibited significantly higher peak currents as compared to the glass carbon mostly likely because their large surface areas can accommodate more electrochemically active sites. Among all three OMC spheres, OMGCS-7 showed the highest activity, which once again confirmed that a high surface area, large pore volume, and sufficient graphitization are essential factors affecting the electrochemical performance. The redox peaks for OMCS-8, OMGCS-7, and OMGCS-8 did not coincide with each other, and no clear trends are visible. This is likely because the chemical nature for the active sites on these carbons is different, leading to various driving forces needed for these redox reactions.

Conclusions

This work shows a facile route to obtain nitrogen-doped mesoporous carbon spheres by combining one-pot synthesis with single-step carbonization. First, we demonstrated the synthesis of core-shell type structures with single PB-cores and phenolic resin-shells by a simple one-pot method using cubic-PB particles and resol polymers. Carbonization of these composites resulted in carbon particles with graphitic domains having several layers of graphene (\sim 11 layers), high pore volume (0.45 cm³ g⁻¹), and embedded nanosized iron particles. The mesopores created during graphitization of the aforementioned carbons showed a broad distribution. Therefore, in the second series of samples mesoporosity was created using the thermally decomposable Pluronic F127 block copolymer, while uniform graphitization was achieved by incorporating relatively small PB nanoparticles as graphitization catalysts. The resulting carbon particles possessed relatively narrow distributions of mesopores, uniform graphitization and well-dispersed nanosized iron species. These nitrogen-doped mesoporous carbon spheres with multiple favorable properties exhibited excellent electrochemical performance, which makes them attractive for energy storage.

Conflicts of interest

There are no conflicts to declare.

Acknowledgements

The TEM data were obtained at the (cryo) TEM facility, Advanced Materials and Liquid Crystal Institute, Kent State University, supported by the Ohio Research Scholars Program Research Cluster on Surfaces in Advanced Materials. The authors thank Dr Min Gao for technical support with TEM imaging. Dr Seval Gunduz and Dr Umit Ozkan at Ohio State University are acknowledged for the support with Raman spectroscopy measurements.

References

1 Y. Zhu, S. Murali, W. Cai, X. Li, J. W. Suk, J. R. Potts and R. S. Ruoff, *Adv. Mater.*, 2010, **22**, 3906–3924.

- 2 L. L. Zhang and X. S. Zhao, *Chem. Soc. Rev.*, 2009, **38**, 2520–2531.
- 3 A. Reina, X. Jia, J. Ho, D. Nezich, H. Son, V. Bulovic, M. S. Dresselhaus and J. Kong, *Nano Lett.*, 2008, **9**, 30–35.
- 4 A. Malesevic, R. Vitchev, K. Schouteden, A. Volodin, L. Zhang, G. Van Tendeloo, A. Vanhulsel and C. Van Haesendonck, *Nanotechnology*, 2008, **19**, 305604.
- 5 J. Zhao, Y. Jiang, H. Fan, M. Liu, O. Zhuo, X. Wang, Q. Wu, L. Yang, Y. Ma and Z. Hu, Adv. Mater., 2017, 29, 1604569.
- 6 J. J. Yoo, K. Balakrishnan, J. Huang, V. Meunier, B. G. Sumpter, A. Srivastava, M. Conway, A. L. Mohana Reddy, J. Yu and R. Vajtai, *Nano Lett.*, 2011, 11, 1423–1427.
- 7 N. Xiao, D. Lau, W. Shi, J. Zhu, X. Dong, H. H. Hng and Q. Yan, *Carbon*, 2013, 57, 184–190.
- 8 S. Wang, J. Zhang, P. Shang, Y. Li, Z. Chen and Q. Xu, *Chem. Commun.*, 2014, **50**, 12091–12094.
- 9 J. Han, G. Xu, B. Ding, J. Pan, H. Dou and D. R. MacFarlane, *J. Mater. Chem. A*, 2014, **2**, 5352–5357.
- 10 Z. Wu, W. Li, Y. Xia, P. Webley and D. Zhao, *J. Mater. Chem.*, 2012, 22, 8835–8845.
- 11 J.-S. Lee, S.-I. Kim, J.-C. Yoon and J.-H. Jang, *ACS Nano*, 2013, 7, 6047–6055.
- 12 X. Chen, K. Kierzek, K. Cendrowski, I. Pelech, X. Zhao, J. Feng, R. J. Kalenczuk, T. Tang and E. Mijowska, *Colloids Surf.*, A, 2012, 396, 246–250.
- 13 W. C. Yen, Y. Z. Chen, C. H. Yeh, J. H. He, P. W. Chiu and Y. L. Chueh, *Sci. Rep.*, 2014, 4, 4739.
- 14 M. B. Vazquez-Santos, E. Geissler, K. László, J. N. Rouzaud, A. Martínez-Alonso and J. M. Tascón, *Carbon*, 2012, 50, 2929–2940.
- M. N. Patel, X. Wang, D. A. Slanac, D. A. Ferrer, S. Dai,
 K. P. Johnston and K. J. Stevenson, *J. Mater. Chem.*, 2012,
 22, 3160–3169.
- 16 S. B. Yoon, G. S. Chai, S. K. Kang, J. S. Yu, K. P. Gierszal and M. Jaroniec, J. Am. Chem. Soc., 2005, 127, 4188–4189.
- 17 P. Su, L. Jiang, J. Zhao, J. Yan, C. Li and Q. Yang, *Chem. Commun.*, 2012, **48**, 8769–8771.
- 18 S. Guo, G. Zhang, Y. Guo and C. Y. Jimmy, *Carbon*, 2013, **60**, 437–444.
- 19 D. Zhai, H. Du, B. Li, Y. Zhu and F. Kang, *Carbon*, 2011, **49**, 725–729.
- 20 A. Oya and S. Otani, Carbon, 1979, 17, 131-137.
- 21 T. Kim, G. Jung, S. Yoo, K. S. Suh and R. S. Ruoff, *ACS Nano*, 2013, 7, 6899–6905.
- 22 D. Pech, M. Brunet, H. Durou, P. Huang, V. Mochalin, Y. Gogotsi, P. L. Taberna and P. Simon, *Nat. Nanotechnol.*, 2010, 5, 651.
- 23 S. Zhao, T. Yan, H. Wang, G. Chen, L. Huang, J. Zhang, L. Shi and D. Zhang, *Appl. Surf. Sci.*, 2016, **369**, 460–469.
- 24 Q. He, Z. Wu and C. Huang, J. Nanosci. Nanotechnol., 2012, 12, 2943–2954.
- 25 N. P. Wickramaratne and M. Jaroniec, *J. Mater. Chem. A*, 2013, **1**, 112–116.
- 26 N. P. Wickramaratne and M. Jaroniec, ACS Appl. Mater. Interfaces, 2013, 5, 1849–1855.
- 27 N. P. Wickramaratne, J. Xu, M. Wang, L. Zhu, L. Dai and M. Jaroniec, *Chem. Mater.*, 2014, 26, 2820–2828.

- 28 N. P. Wickramaratne, V. S. Perera, J. M. Ralph, S. D. Huang and M. Jaroniec, *Langmuir*, 2013, 29, 4032–4038.
- 29 R. Ghosh Chaudhuri and S. Paria, *Chem. Rev.*, 2011, **112**, 2373–2433.
- 30 J. Tang, T. Wang, X. Sun, Y. Guo, H. Xue, H. Guo, M. Liu, X. Zhang and J. He, *Microporous Mesoporous Mater.*, 2013, 177, 105–112.
- 31 N. Zhu, S. Han, S. Gan, J. Ulstrup and Q. Chi, *Adv. Funct. Mater.*, 2013, 23, 5297–5306.
- 32 Y. Hu, J. O. Jensen, W. Zhang, L. N. Cleemann, W. Xing, N. J. Bjerrum and Q. Li, *Angew. Chem., Int. Ed. Engl.*, 2014, 53, 3675–3679.
- 33 S. E. Gratton, P. A. Ropp, P. D. Pohlhaus, J. C. Luft, V. J. Madden, M. E. Napier and J. M. DeSimone, *Proc. Natl. Acad. Sci. U. S. A.*, 2008, **105**, 11613–11618.
- 34 B. Y. Guan, S. L. Zhang and X. W. Lou, *Angew. Chem., Int. Ed. Engl.*, 2018, **130**, 6284–6288.
- 35 X. Liu, W. Li and S. Zou, *J. Mater. Chem. A*, 2018, **6**, 17067–17074.
- 36 P. Ghimire, C. Gunathilake, N. P. Wickramaratne and M. Jaroniec, *Carbon*, 2017, **121**, 408–417.
- 37 M. R. Benzigar, S. Joseph, H. Ilbeygi, D. H. Park, S. Sarkar, G. Chandra, S. Umapathy, S. Srinivasan, S. N. Talapaneni and A. Vinu, *Angew. Chem., Int. Ed. Engl.*, 2018, 130, 578–582.
- 38 H. Zhou, S. Zhu, M. Hibino, I. Honma and M. Ichihara, *Adv. Mater.*, 2003, **15**, 2107–2111.
- 39 W. E. Kline and H. S. Fogler, *Ind. Eng. Chem. Res.*, 1981, 20, 155–161.
- 40 J. H. Bang, Electrochim. Acta, 2011, 56, 8674-8679.
- 41 S. X. Wang, S. Chen, Q. Wei, X. Zhang, S. Y. Wong, S. Sun and X. Li, *Chem. Mater.*, 2014, 27, 336–342.
- 42 B. Y. Guan, L. Yu and X. W. Lou, Adv. Mater., 2016, 28, 9596–9601.
- 43 D. Liu, N. Xue, L. Wei, Y. Zhang, Z. Qin, X. Li, B. P. Binks and H. Yang, *Angew. Chem., Int. Ed. Engl.*, 2018, 57, 10899–10904.
- 44 N. P. Wickramaratne, V. S. Perera, B. W. Park, M. Gao, G. W. McGimpsey, S. D. Huang and M. Jaroniec, *Chem. Mater.*, 2013, 25, 2803–2811.
- 45 A. Chen, Y. Yu, T. Xing, R. Wang, Y. Zhang and Q. Li, *J. Mater. Sci.*, 2015, **50**, 5578–5582.
- 46 H. Ming, A. A. Belik, M. Imura, K. Mibu, Y. Tsujimoto and Y. Yamauchi, *Chem. Mater.*, 2012, **24**, 2698–2707.
- 47 F. Ricci, A. Amine, G. Palleschi and D. Moscone, *Biosens. Bioelectron.*, 2003, **18**, 165–174.
- 48 M. Hu, J. S. Jiang and Y. Zeng, Chem. Commun., 2010, 46, 1133-1135.
- 49 P. Van Der Voort, C. Vercaemst, D. Schaubroeck and F. Verpoort, *Phys. Chem. Chem. Phys.*, 2008, **10**, 347–360.
- 50 Q. Li, R. Jiang, Y. Dou, Z. Wu, T. Huang, D. Feng, J. Yang, A. Yu and D. Zhao, *Carbon*, 2011, 49, 1248–1257.
- 51 T. Yang, J. Liu, R. Zhou, Z. Chen, H. Xu, S. Z. Qiao and M. J. Monteiro, *J. Mater. Chem. A*, 2014, 2, 18139–18146.
- 52 Y. Chen, B. Song, M. Li, L. Lu and J. Xue, *Adv. Funct. Mater.*, 2014, 24, 319–326.
- 53 J. G. Wang, H. Liu, H. Sun, W. Hua, H. Wang, X. Liu and B. Wei, *Carbon*, 2018, **127**, 85–92.

- 54 Y. Yan, F. Zhang, Y. Meng, B. Tu and D. Zhao, *Chem. Commun.*, 2007, 2867–2869.
- 55 M. Li and J. Xue, J. Colloid Interface Sci., 2012, 377, 169-175.
- 56 A. Sadezky, H. Muckenhuber, H. Grothe, R. Niessner and U. Pöschl, *Carbon*, 2005, 43, 1731–1742.
- 57 T. Palaniselvam, H. B. Aiyappa and S. Kurungot, *J. Mater. Chem.*, 2012, 22, 23799–23805.
- 58 M. Thommes, K. Kaneko, A. V. Neimark, J. P. Olivier, F. Rodriguez-Reinoso, J. Rouquerol and K. S. Sing, *Pure Appl. Chem.*, 2015, **87**, 1051–1069.
- 59 J. K. Park, J. Jung, P. Subramaniam, B. P. Shah, C. Kim, J. K. Lee, J. H. Cho, C. Lee and K. B. Lee, *Small*, 2011, 7, 1647–1652.
- 60 X. Yang, X. Zhang, Y. Ma, Y. Huang, Y. Wang and Y. Chen, *J. Mater. Chem.*, 2009, **19**, 2710–2714.
- 61 J. Yan, *Handbook of Clean Energy Systems, 6 Volume Set*, John Wiley & Sons, 2015.

- 62 T. Liu, L. Zhang, B. Cheng and J. Yu, *Adv. Energy Mater.*, 2019, 1803900.
- 63 Z. S. Wu, Y. Sun, Y. Z. Tan, S. Yang, X. Feng and K. Müllen, *J. Am. Chem. Soc.*, 2012, 134, 19532–19535.
- 64 L. Zhou, H. Li, C. Yu, X. Zhou, J. Tang, Y. Meng, Y. Xia and D. Zhao, *Carbon*, 2006, **8**, 1601–1604.
- 65 T. Yang, R. Zhou, D. W. Wang, S. P. Jiang, Y. Yamauchi, S. Z. Qiao, M. J. Monteiro and J. Liu, *Chem. Commun.*, 2015, 51, 2518–2521.
- 66 X. Shi, S. Zhang, X. Chen, T. Tang and E. Mijowska, *J. Alloys Compd.*, 2017, **726**, 466–473.
- 67 Z. C. Yang, C. H. Tang, H. Gong, X. Li and J. Wang, *J. Power Sources*, 2013, **240**, 713–720.
- 68 W. Xu, H. Shen, Y. J. Kim, X. Zhou, G. Liu, J. Park and P. Chen, *Nano Lett.*, 2009, **9**, 3968–3973.
- 69 S. M. Oja, J. P. Guerrette, M. R. David and B. Zhang, *Anal. Chem.*, 2014, **86**, 6040–6048.